

Single-Layer BI: A Multifunctional Semiconductor with Ferroelectricity, Ultrahigh Carrier Mobility, and Negative Poisson's Ratio

Shiying Shen, Qian Wu, Yan Liang, Baibiao Huang, Ying Dai,* and Yandong Ma†

School of Physics, State Key Laboratory of Crystal Materials, Shandong University, Shandan Street 27, Jinan 250100, People's Republic of China



(Received 6 October 2020; revised 24 November 2020; accepted 22 December 2020; published 15 January 2021)

Developing two-dimensional multifunctional materials is highly desirable for nanoscale device applications. Herein, by means of first-principles calculations, we demonstrate a promising two-dimensional multifunctional semiconductor with ferroelectricity, ultrahigh carrier mobility, and negative Poisson's ratio in single-layer BI. We show that single-layer BI exhibits intrinsic ferroelectricity, derived from its asymmetric structure, and the ferroelectricity features an in-plane electric polarization as large as $3.3 \times 10^{-10} \text{ C m}^{-1}$, which is beneficial for nonvolatile memories. Owing to its large band dispersion, single-layer BI is also found to harbor an extremely high carrier mobility ($1.17 \times 10^5 \text{ cm}^2 \text{ V}^{-1} \text{ s}^{-1}$), even comparable to that of graphene, suggesting its potential for high-performance electronics and bulk photovoltaic effect. This, combined with the moderate band gap, renders single-layer BI with a high absorption coefficient (10^5 cm m^{-1}) from near-infrared to ultraviolet light. In addition, we unveil that single-layer BI is a long-sought-after auxetic material with a negative Poisson's ratio of -0.31 . All of these findings make single-layer BI a compelling multifunctional material, offering a versatile platform for diverse nanoscale devices applications.

DOI: 10.1103/PhysRevApplied.15.014027

I. INTRODUCTION

Multifunctional materials, allowing integration of highly distinct properties, have attracted considerable attention [1,2] because they provide a unique opportunity to address questions of fundamental and practical importance. This is particularly interesting in two-dimensional (2D) limit, in light of the fact that 2D materials show rich and varied electric, optoelectric, and mechanical behaviors [3]. Among various properties of 2D materials, 2D ferroelectric (FE) order receives special attention, considering its potential for miniaturized electronic and memory devices. Currently, several 2D FE materials have been proposed, including FE graphanol [4], Group IV monochalcogenides [5–10], 1T-phase MoS₂ [11], Group V materials [12–16], VO₂I₄ [17], MO₂X₂ [18], and NbOX₂ [19]. Nonetheless, stable FE order is only found in a small number of 2D materials by experiments, to date, i.e., Chang *et al.* and Zhou *et al.*, respectively, confirmed the robust ferroelectricity in monolayer SnTe [20] and In₂Se₃ nanoflakes [21]. It is therefore crucial to design 2D FE materials, especially those with large electric polarization.

When endowing 2D FE materials with ultrahigh carrier mobility, the high-performance bulk photovoltaic effect

(BPVE), referring to the conversion of solar energy into photocurrents, can be expected [22]. Different from conventional solar cells, the BPVE can generate an above-band-gap photovoltage, without a built-in potential at a *p-n* junction, to separate photoexcited carriers. Moreover, the photoconversion efficiency of the BPVE is not restricted by the Shockley-Queisser limit [23–25]. Given these merits, the BPVE is extremely promising for exploring high-performance solar cells. Although highly valuable and principally allowable, the BPVE is rarely reported in 2D FE materials [26,27]. This is because the simultaneous presence of ultrahigh carrier mobility in 2D FE materials is challenging, i.e., most of the previously reported 2D FE materials consist of metal elements and such systems frequently present a low carrier mobility.

Another intriguing phenomenon that has received growing attention at the 2D limit is auxetic behavior. In conventional 2D materials, the Poisson's ratio, an important parameter to evaluate the mechanical properties, is positive with values in the range of 0 to 0.5 [28,29]. By contrast, 2D auxetic materials present a negative Poisson's ratio (NPR), that is, they tend to expansion (contraction) in the transverse direction upon applying a tensile (compressive) strain in the longitudinal direction. Such an unusual feature enables 2D auxetic materials with promoted mechanical properties (enhanced toughness, shear modulus, vibration absorption, and indentation resistance) [30], thus resulting in potential applications in the fields

*daiy60@sdu.edu.cn

†yandong.ma@sdu.edu.cn

of national security, biomedicine, sensors, and defense. So far, only limited cases are reported to be in this class of materials, such as Zn_2C , PtI_2 , Ag_2S , Be_5C_2 , and δ -phosphorene [31–35]. It is of profound interest to explore 2D auxetic materials.

Herein, we report that single-layer (SL) BI is an intriguing 2D multifunctional semiconductor, allowing for the simultaneous presence of ferroelectricity, ultrahigh carrier mobility, and negative Poisson's ratio. SL BI is identified to be dynamically, thermally, and mechanically stable. Arising from its particular crystal symmetry, SL BI is an excellent candidate for achieving 2D ferroelectricity, as it shows a large in-plane electric polarization of $3.3 \times 10^{-10} \text{ C m}^{-1}$ and a moderate FE transition barrier of 48.5 meV/unit cell. Moreover, SL BI presents a significantly high carrier mobility of $1.17 \times 10^5 \text{ cm}^2 \text{ V}^{-1} \text{ s}^{-1}$, which is even comparable with that of graphene. In addition, SL BI is revealed to show a negative Poisson's ratio of -0.31 , suggesting it is also a long-sought-after 2D auxetic material. The simultaneous presence of these seemingly incompatible properties not only offers a versatile platform for diverse applications, but also enables future studies to explore the interplay between them as well as applications.

II. COMPUTATIONAL DETAILS

All calculations are performed by using density-functional theory (DFT), as implemented in the Vienna *ab initio* simulation package [36,37]. The exchange correlation is treated by the Perdew-Burke-Ernzerhof (PBE) functional within the generalized gradient approximation (GGA) [38]. The cutoff energy is set to 500 eV. Monkhorst-Pack k grids of $7 \times 7 \times 1$ are used to sample the Brillouin zone. To eliminate spurious interlayer interactions, a vacuum space along the z direction is set to 20 Å. The van der Waals interactions are described using DFT-D3 [39]. As the PBE functional usually underestimates the band gap, we adopt the Heyd-Scuseria-Ernzerhof (HSE06) hybrid functional to calculate the band structure [40]. Structures are fully optimized until residual forces and energies converge with an accuracy of 0.01 eV/Å and 10^{-5} eV, respectively. The spontaneous polarization, P_s , is calculated using the Berry phase approach. The climbing-image nudged-elastic band (cNEB) method is employed to calculate the transition states and minimum energy path [41]. *Ab initio* molecular dynamics (AIMD) simulations are performed with a $3 \times 3 \times 1$ supercell at 300 K with a time step of 1 fs for 5 ps. Phonon calculations are carried out by using the PHONOPY code [42]. The band structure and electric polarizations with spin-orbital coupling (SOC) are shown in Figs. S1 and S2 within the Supplemental Material [43], from which we can see that the SOC effect is negligible. Therefore, in this work, we neglect the SOC effect.

III. RESULTS AND DISCUSSION

Figure 1(a) shows the crystal structure of SL BI. The unit cell of SL BI consists of four B atoms and four I atoms, featuring an orthorhombic lattice with $Abm2$ symmetry. Therefore, SL BI is noncentrosymmetric. The lattice constants are optimized to be $a = 5.44$ and $b = 5.40$ Å. Each I atom coordinates with five B atoms and vice versa. Due to the off-centering displacements of B and I atoms, there are four groups of B—I bonds with bond lengths of 2.381, 2.481, 2.747, and 2.949 Å [see Fig. 1(a)]. To reflect the bonding character in SL BI, the ELF map is plotted in Fig. 1(b). It can be seen that electrons mainly distribute at the B and I sites, as well as around the centers between them, implying a covalent character of the B—I bond.

To ascertain the dynamic stability of SL BI, we calculate its phonon band dispersions. As shown in Fig. 1(d), there is no imaginary frequency over the whole Brillouin zone, indicating its dynamic stability. We further assess the thermal stability of SL BI by carrying out AIMD simulations. As displayed in Fig. 1(e), the free energy of SL BI fluctuates slightly during the annealing process at 300 K for 5 ps, and the crystal structure exhibits neither broken bonds nor structural reconstruction during the simulation, which confirms the thermal stability of SL BI. We also calculate the formation energy of SL BI based on $E_f = (E_{BI} - 4\mu_B - 4\mu_I)/8$, where E_{BI} , μ_B , and μ_I denote the total energy of SL BI, the chemical potential for the B atom taken from borophene, and the chemical potential for I atom taken from I_2 molecule, respectively. The formation energy is estimated to be -0.26 eV/atom, and this negative value indicates the stability of SL BI. It is known that a mechanically stable 2D structure must obey the Born criteria [44], $C_{11}C_{22} - C_{12}^2 > 0$ and $C_{66} > 0$, where C_{ij} are the elastic constants. The calculated elastic constants of SL BI are $C_{11} = 58.5$, $C_{22} = 47.7$, $C_{12} = -14.8$, and $C_{66} = 36.7$ N/m, which obviously satisfy the Born criteria, suggesting that SL BI is mechanically stable. Given these facts, SL BI is expected to be experimentally fabricated, especially considering that ultrathin InI flakes have been successfully grown [45].

As mentioned above, B and I atoms are intrinsically off-centering displaced along the b direction; see Fig. 1(a). Considering the large difference in electronegativity between B and I atoms, such off-centering displacement is expected to give rise to spontaneous electric polarization (P_s) along the b direction, as well as 2D ferroelectricity. To confirm this, we first study the electric polarization of SL BI following the ways of modern theory of polarization, especially using the Berry phase approach. Here, the structure with B and I atoms that are coincident, namely, the positive and negative charges are coincident, is regarded as the paraelectric (PE) state, which shows $cmma$ symmetry. As depicted in Fig. S1 within the Supplemental Material [43], SL BI exhibits a spontaneous

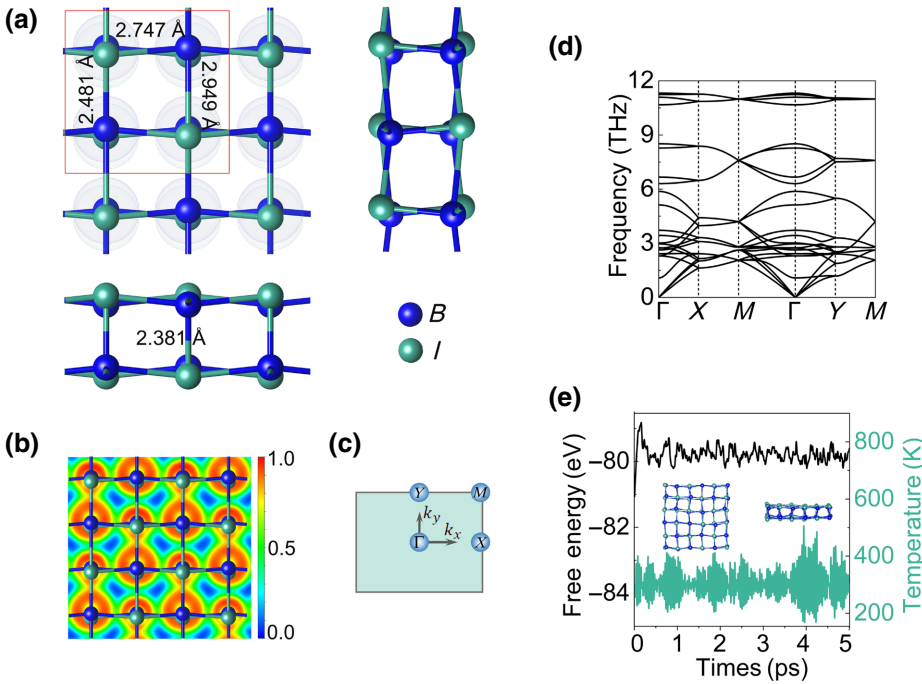


FIG. 1. (a) Top and side views of the crystal structure of SL BI with red lines highlighting the unit cell. (b) Electron localization function (ELF) of SL BI, wherein red and blue areas indicate accumulated and vanishing electron density, respectively. (c) 2D Brillouin zone of SL BI. (d) Phonon band dispersions for SL BI. (e) Variations of the total energy of SL BI during AIMD simulations at 300 K. Insets in (e) show snapshots of the structure taken from the end of the AIMD simulation at 300 K.

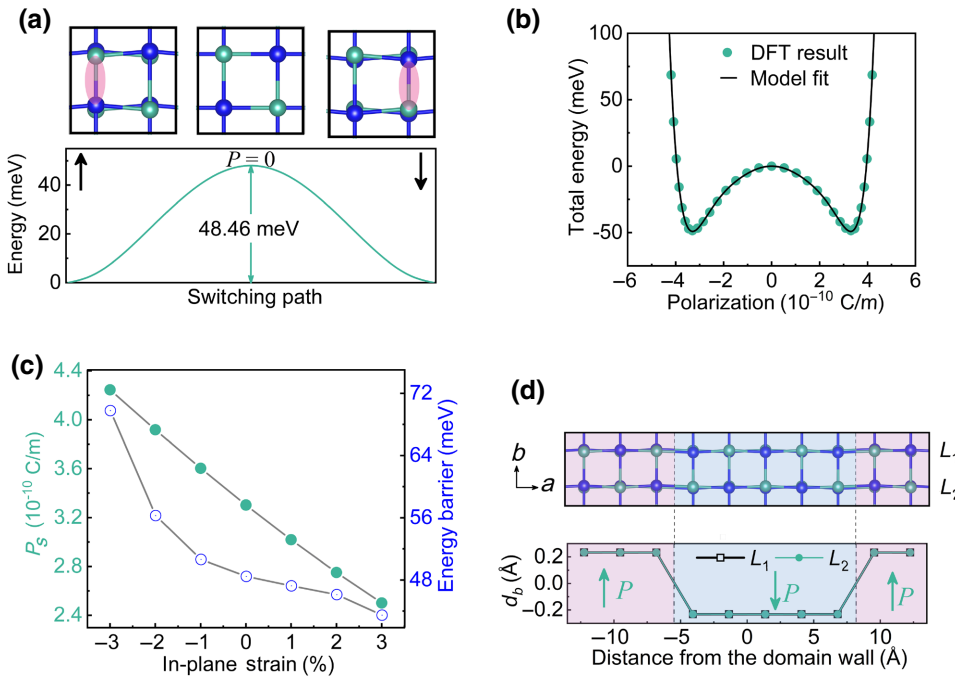
in-plane electric polarization, P_s , of $3.3 \times 10^{-10} \text{ C m}^{-1}$ along the b direction. This value is much larger than those of well-known 2D FE materials, e.g., SL AgBiP₂Se₆ ($1.2 \times 10^{-12} \text{ C m}^{-1}$) [46], Hf₂VC₂F₂ ($1.95 \times 10^{-12} \text{ C m}^{-1}$) [47], and SnTe ($1.94 \times 10^{-10} \text{ C m}^{-1}$) [10], which is beneficial for practical applications. Moreover, the electric polarization P_s of SL BI is along the in-plane direction, which would overcome the problems of the depolarization field faced in the out-of-plane case.

The existence of electric polarization does not guarantee its switchable ability, namely, ferroelectricity. To this end, we further investigate the FE switching barrier of SL BI using the cNEB method. The corresponding results are shown in Fig. 2(a). We can see that the energy barrier, E_b , for FE switching in SL BI is 48.5 meV/unit cell. This is larger than that of β-GeSe (11.66 meV/unit cell) [48] and SnSe (3.76 meV/unit cell) [10], but smaller than that of Sc₂CO₂ (0.52 eV/unit cell) [1] and GaTeCl (0.75 eV/unit cell) [3]. Such a moderate switching barrier highlights the rational FE switching in SL BI under an external electric field and robustness against environmental perturbation. The energy versus polarization P_s of SL BI is plotted in Fig. 2(b), from which we can see the anharmonic double-well potential, firmly confirming its 2D FE feature [49]. We also investigate the strain effect on the FE performances of SL BI. The in-plane strain-dependent spontaneous electric polarization, P_s , and energy barrier, E_b , of SL BI are shown in Fig. 2(c). Clearly, both spontaneous electric polarization, P_s , and energy barrier, E_b , present significant variation upon applying strain. For example, by increasing the biaxial strain from -3% to 3% , the spontaneous polarization, P_s , reduces from 4.25×10^{-10} to

$2.50 \times 10^{-10} \text{ C m}^{-1}$. This indicates that strain is a feasible way to engineer ferroelectricity in SL BI.

To gain a further insight into the 2D ferroelectricity of SL BI, we study its FE domain wall. Concerning its electric polarization directions, 180° FE domain walls between oppositely orientated FE domains for SL BI are constructed, see Fig. 2(d). To characterize the effect of the domain wall on electric polarization, we employ the polar displacement of the B atom along the b axis, d_b . The evaluation of d_b as a function of the distance from the domain wall is summarized in Fig. 2(d). We can see that, in the same domain, d_b remains almost the same when changing the distance, and d_b experiences an abrupt change when crossing the domain wall. As the polarization reversal process is realized through the motion of FE domain walls in practice, the corresponding minimum-energy-pathway trajectory for domain-wall motion in SL BI is explored. As shown in Fig. S3 within the Supplemental Material [43], for the saddle-point configuration, the intermediate PE phase, where d_b is constrained to have zero polar displacement, separates two distinct FE domains. The overall energy barrier for this polarization reversal is found to be 6.03 meV, which is much smaller than that of PbTiO₃ (40 meV) [50], suggesting that domain-wall motion in SL BI is feasible.

Figure 3(a) shows the band structure and projected density of states (PDOS) of SL BI. Obviously, SL BI is an indirect gap semiconductor with a band gap of 0.52 eV. This suggests that SL BI is a 2D FE semiconductor. Both the valence-band maximum (VBM) and conduction-band minimum (CBM) are located between the Γ and M points. Our PDOS reveals that the VBM is mainly composed of



B 2s, B 2p, and I 5p states, while the CBM is dominantly contributed to by B 2p states. This agrees well with the partial charge density analysis shown in Fig. S4 within the Supplemental Material [43]. Figure S5 within the Supplemental Material [43] presents the band structures of SL BI under various biaxial strains. It can be seen that, upon increasing the strain from -3% to 3% , the band gap of SL BI increases monotonously.

Another interesting point in the band structure of SL BI we wish to stress is that the low-energy bands are highly dispersed. This is significantly different from that of most previously reported 2D FE materials, wherein the low-energy bands are less dispersed [3,46]. Such band dispersions probably give rise to a small carrier effective mass and a high carrier mobility, which are suitable for optoelectronics. As FE materials exhibit the BPVE, when endowing SL BI with ultrahigh carrier mobility, the observation of a high-performance BPVE can be expected. To this end, we first investigate the carrier effective mass of SL BI, according to the following equation:

$$m^* = \pm \hbar^2 \left(\frac{d^2 E_k}{dk^2} \right)^{-1}. \quad (1)$$

Here, \mathbf{k} is the wave vector and E_k is the energy corresponding to the wave vector \mathbf{k} . As listed in Table I, the effective masses of electrons and holes along the x direction are 0.05 and $0.06 m_0$ (m_0 is the mass of free electron), respectively, while they are 0.52 and $0.13 m_0$, respectively, in the y direction. This means that SL BI exhibits a significant anisotropy in the carrier effective mass. Particularly for the electron effective masses, the anisotropy ratio is

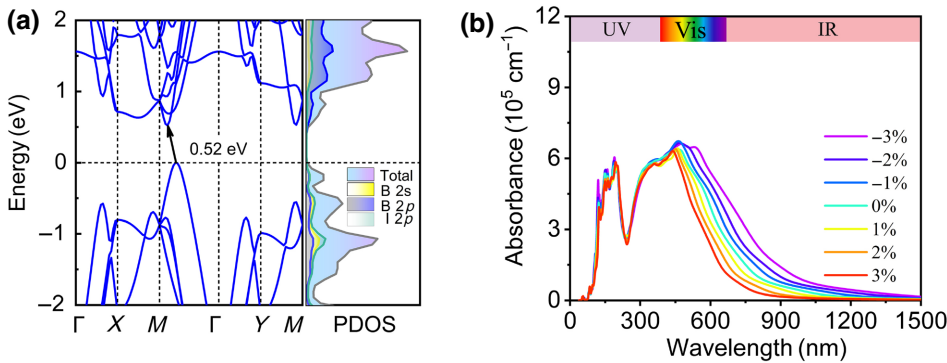
FIG. 2. (a) Minimum-energy pathway, along with corresponding structures, of FE-PE-FE transition in SL BI obtained from the cNEB calculation; corresponding shortest B—I bonds in the 2D plane are highlighted in pink. (b) Double-well potential versus polarization of SL BI. (c) Energy barrier and polarizations as a function of in-plane strain for SL BI. (d) FE domain walls of SL BI (d_b are displacements along the $+b$ axis).

up to 10.4 , which is significantly higher than that of *t*-YN (2.94) and phosphorene (6.59) [51]. Such large anisotropy ratios indicate remarkable anisotropic behavior in the carrier transport of SL BI. Moreover, the carrier effective masses of SL BI are generally smaller than those of most previously reported 2D FE materials, which might yield an excellent transport performance.

To explore the transport properties of SL BI, we calculate its carrier mobility using deformation potential (DP) theory at room temperature [52]:

$$\mu = \frac{2e\hbar^3 C}{3K_B T m^* m_d E_d^2}. \quad (2)$$

Here, e , K_B , m^* , and T are the electron charge, Boltzmann constant, carrier effective mass, and temperature, respectively. $m_d = \sqrt{m_x^* m_y^*}$ is the average effective mass. $C = [\partial^2 E / \partial \varepsilon^2]/S$ is the elastic modulus of SL BI activated by strain, where E is the total energy and S is the area of the system. E_d is the DP constant denoting the shift of the band edges (E_{edge}) (CBM for electrons and VBM for holes) induced by strain, which can be expressed as $E_d = dE_{\text{edge}}/d\varepsilon$. The strain ε is defined as $\varepsilon = \Delta l/l_0$, where Δl and l_0 are the change of the lattice constant and the primary lattice constant, respectively. The corresponding results are summarized in Table I. We can see that electron mobility along the x direction is $1.17 \times 10^5 \text{ cm}^2 \text{ V}^{-1} \text{ s}^{-1}$, which is two orders of magnitude larger than the hole mobility ($3.77 \times 10^3 \text{ cm}^2 \text{ V}^{-1} \text{ s}^{-1}$). While for the y direction, the electron mobility is $0.86 \times 10^5 \text{ cm}^2 \text{ V}^{-1} \text{ s}^{-1}$ and the hole mobility is $1.08 \times 10^4 \text{ cm}^2 \text{ V}^{-1} \text{ s}^{-1}$. Accordingly, electron transport in SL BI is facilitated along the x direction, while the y direction favors hole transport. Aside from



the anisotropic feature, we also wish to emphasize that both hole and electron mobilities for SL BI are much higher than that of MoS₂ ($320 \text{ cm}^2 \text{ V}^{-1} \text{ s}^{-1}$) and black phosphorene ($2.2 \times 10^3 \text{ cm}^2 \text{ V}^{-1} \text{ s}^{-1}$), and even comparable to that in graphene ($3.2 \times 10^5 \text{ cm}^2 \text{ V}^{-1} \text{ s}^{-1}$) [53–55]. Such ultrahigh carrier mobility, accompanied by the intrinsic ferroelectricity, suggest that SL BI is a promising candidate for achieving the high-performance BPVE.

Given the high carrier mobility as well as the narrow band gap, we also assess the optical performance of SL BI by calculating the absorption coefficients based on the following equation [56]:

$$\alpha(\omega) = \sqrt{2} \frac{\omega}{c} \left[\sqrt{\varepsilon_1^2(\omega) + \varepsilon_2^2(\omega)} - \varepsilon_1(\omega) \right]^{1/2} \quad (3)$$

Here, ε_1 and ε_2 are the real and imaginary parts of the dielectric function, respectively. As shown in Fig. 3(b), SL BI exhibits a remarkably high absorbance coefficient (10^5 cm^{-1}) and broad-wavelength range of optical absorption from near-infrared to ultraviolet. These properties are even superior to those of MoS₂ [57]. We further investigate the optical absorption of SL BI under different lattice distortions to evaluate the light-absorption ability. As illustrated in Fig. 3(b), with increasing compressive strain and tensile strain, the absorption edge exhibits a redshift first and then a blueshift, in good accordance with the band-gap variation.

Finally, we discuss the mechanical properties of SL BI. Based on the calculated elastic constants, the Young's modulus, $Y(\theta)$, and Poisson's ratio, $\nu(\theta)$, along an arbitrary

TABLE I. In-plane stiffness, effective mass, deformation potential, and carrier mobility of SL BI.

Carrier type	Direction	C (N m^{-1})	m^* (m_e)	E_d (eV)	μ ($\text{cm}^2 \text{ V}^{-1} \text{ s}^{-1}$)
Electron	x	52.75	0.05	0.79	1.17×10^5
	y	52.68	0.52	3.09	0.86×10^3
Hole	x	52.75	0.06	6.09	3.77×10^3
	y	52.68	0.13	2.44	1.08×10^4

FIG. 3. (a) Band structure and projected density of states for SL BI. Fermi level is set to 0 eV. (b) Optical absorption coefficients of SL BI under strain from -3% to 3%.

in-plane θ can be expressed as follows [58]:

$$Y(\theta) = \frac{C_{11}C_{22} - C_{12}^2}{C_{22}\cos^4\theta + A\cos^2\theta\sin^2\theta + C_{11}\sin^4\theta} \quad (4)$$

$$\nu(\theta) = \frac{C_{12}(\cos^4\theta + \sin^4\theta) - B\cos^2\theta\sin^2\theta}{C_{22}\cos^4\theta + A\cos^2\theta\sin^2\theta + C_{11}\sin^4\theta}. \quad (5)$$

Here, $A = (C_{11}C_{22} - C_{12}^2)/C_{66} - 2C_{12}$ and $B = C_{11} + C_{22} - (C_{11}C_{22} - C_{12}^2)/C_{66}$. The calculated Young's modulus, $Y(\theta)$, of SL BI is plotted in Fig. 4(a). It can be seen that the Young's modulus varies from 23.2 to 53.9 N/m, indicating mechanical anisotropy, which arises from the asymmetric crystal structure of SL BI. Although the Young's modulus is less than that of graphene (340 N/m) and MoS₂ (128 N/m), it is comparable to that of phosphorene (23–92 N/m) and silicene (62 N/m) [59–62]. As the Young's modulus reflects the fully reversible stiffness response, these values establish that SL BI has moderate rigidity against deformation.

Different from the Young's modulus, the Poisson's ratio is defined as the negative ratio of the transverse strain to the corresponding axial strain, which characterizes a material's resultant strain in the longitudinal direction for a material under transverse stress. Figure 4(b) displays the calculated Poisson's ratio of SL BI. We can see that the Poisson's ratio of SL BI presents an anisotropic feature. More interestingly, SL BI exhibits a NPR along the axial directions and reaches its maximum value of -0.31 in the x direction. To confirm the unusual NPR in SL BI, we apply uniaxial tensile strains. As shown in Fig. S6 within the Supplemental Material [43], when stretched (compressed) along the x direction, SL BI expands (contracts) along the y direction, which agrees well with the above analysis. Currently, materials with a NPR are scarce, as nearly all materials possess positive Poisson ratios in nature [31–35]. Even for the few existing materials with a NPR, the values are relatively small, making them far from applicable. The presence of a large NPR definitely would entail SL BI being highly useful for mechanical applications.

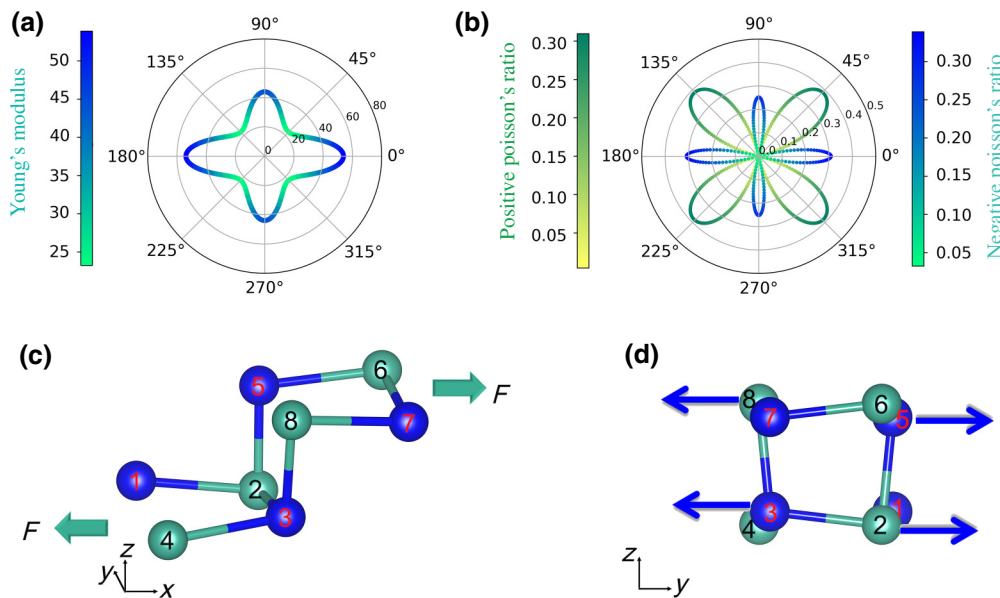


FIG. 4. Polar diagrams of (a) Young's modulus $Y(\theta)$ and (b) Poisson's ratio $\nu(\theta)$ of SL BI. Evolution of local structures of SL in the x - z (c) and y - z (d) planes under uniaxial tension strain.

To explain the origin of the NPR of SL BI, the local skeleton structures of SL BI are presented in Figs. 4(c) and 4(d). Upon imposing tensile strain in the x direction, atoms 1, 4 and 6, 7 will move outward along the x direction. Thus, the angles φ_{125} and φ_{387} are increased, while the angles φ_{438} and φ_{652} are decreased. This results in strain energy being stored in these angles. Due to these bond angles not being in the x - z plane, atoms 2, 3 in the interior of the slab will move outward in the y direction, resulting in the increased bond length, r_{23} , as illustrated in Fig. 4(d). As a consequence, atoms 5, 8 are pushed outward in the y direction, leading to a negative Poisson's ratio. This scenario is applicable to the case of applying strain along the y direction.

IV. CONCLUSIONS

We predict SL BI as a promising 2D multifunctional semiconductor. SL BI presents 2D ferroelectricity intrinsically, exhibiting a high in-plane P_s of about 3.30×10^{-10} C/m and a moderate FE transition barrier of 48.5 meV/unit cell. It shows ultrahigh carrier mobility with anisotropic character. This accompanies the 2D FE feature and makes the BPVE feasible in SL BI. Moreover, SL BI displays a unique NPR with a value as large as -0.31 . The discovery of the simultaneous presence of these intriguing properties in SL BI provides an extraordinary candidate system for exploring multifunctional device applications.

ACKNOWLEDGMENTS

This work is supported by the National Natural Science Foundation of China (Grant No. 11804190), Shandong Provincial Natural Science Foundation of China (Grants No. ZR2019QA011 and No. ZR2019MEM013), Shandong Provincial Key Research and Development

Program (Major Scientific and Technological Innovation Project) (Grant No. 2019JZZY010302), Shandong Provincial Key Research and Development Program (Grant No. 2019RKE27004), Qilu Young Scholar Program of Shandong University, and Taishan Scholar Program of Shandong Province.

The authors declare no competing financial interests.

- [1] A. Chandrasekaran, A. Mishra, and A. K. Singh, Ferroelectricity, antiferroelectricity, and ultrathin 2D electron/hole gas in multifunctional monolayer MXene, *Nano Lett.* **17**, 3290 (2017).
- [2] W. Chen, X. Hou, X. Shi, and H. Pan, Two-dimensional janus transition metal oxides and chalcogenides: Multifunctional properties for photocatalysts, electronics, and energy conversion, *ACS Appl. Mater. Interfaces* **10**, 35289 (2018).
- [3] S. Zhang and B. Liu, A controllable robust multiferroic GaTeCl monolayer with colossal 2D ferroelectricity and desirable multifunctionality, *Nanoscale* **10**, 5990 (2018).
- [4] M. H. Wu, J. D. Burton, E. Y. Tsymbal, X. C. Zeng, and P. Jena, Hydroxyl-decorated graphene systems as candidates for organic metal-free ferroelectrics, multiferroics, and high-performance proton battery cathode materials, *Phys. Rev. B* **87**, 081406 (2013).
- [5] C. Cui, W. J. Hu, X. Yan, C. Addiego, W. Gao, Y. Wang, Z. Wang, L. Li, Y. Cheng, P. Li, X. Zhang, H. N. Alshaaraf, T. Wu, W. Zhu, X. Pan, and L. J. Li, Intercorrelated in-plane and out-of-plane ferroelectricity in ultrathin two-dimensional layered semiconductor In_2Se_3 , *Nano Lett.* **18**, 1253 (2018).
- [6] H. Wang and X. F. Qian, Two-dimensional multiferroics in monolayer group IV monochalcogenides, *2D Mater.* **4**, 015042 (2017).
- [7] W. H. Wan, C. Liu, W. D. Xiao, and Y. G. Yao, Promising ferroelectricity in 2D group IV tellurides: A first-principles study, *Appl. Phys. Lett.* **111**, 132904 (2017).

- [8] M. Wu and X. C. Zeng, Intrinsic ferroelasticity and/or multiferroicity in two-dimensional phosphorene and phosphorene analogues, *Nano Lett.* **16**, 3236 (2016).
- [9] P. Z. Hanakata, A. Carvalho, D. K. Campbell, and H. S. Park, Polarization and valley switching in monolayer group-IV monochalcogenides, *Phys. Rev. B* **94**, 035304 (2016).
- [10] R. Fei, W. Kang, and L. Yang, Ferroelectricity and Phase Transitions in Monolayer Group-IV Monochalcogenides, *Phys. Rev. Lett.* **117**, 097601 (2016).
- [11] J. R. Reimers, S. A. Tawfik, and M. J. Ford, Van der Waals forces control ferroelectric– antiferroelectric ordering in CuInP₂S₆ and CuBiP₂Se₆ laminar materials, *Chem. Sci.* **9**, 7620 (2018).
- [12] C. C. Xiao, F. Wang, S. Y. A. Yang, Y. H. Lu, Y. P. Feng, and S. B. Zhang, Elemental ferroelectricity and antiferroelectricity in group-V monolayer, *Adv. Funct. Mater.* **28**, 1707383 (2018).
- [13] C. Liu, W. Wan, J. Ma, W. Guo, and Y. Yao, Robust ferroelectricity in two-dimensional SbN and BiP, *Nanoscale* **10**, 7984 (2018).
- [14] L. Z. Kou, Y. D. Ma, T. Liao, A. J. Du, and C. F. Chen, Multiferroic and Ferroic Topological Order in Ligand-Functionalized Germanene and Arsenene, *Phys. Rev. Appl.* **10**, 024043 (2018).
- [15] L. Z. Kou, H. X. Fu, Y. D. Ma, B. H. Yan, T. Liao, A. J. Du, and C. F. Chen, Two-dimensional ferroelectric topological insulators in functionalized atomically thin bismuth layers, *Phys. Rev. B* **97**, 075429 (2018).
- [16] S. Y. Shen, C. Liu, Y. M. Ma, B. B. Huang, and Y. Dai, Robust two-dimensional ferroelectricity in singlelayer γ -SbP and γ -SbAs, *Nanoscale* **11**, 11864 (2019).
- [17] C. S. Xu, P. Chen, H. X. Tan, Y. R. Yang, H. J. Xiang, and L. Bellaiche, Electric-Field Switching of Magnetic Topological Charge in Type-I Multiferroics, *Phys. Rev. Lett.* **125**, 037203 (2020).
- [18] L. F. Lin, Y. Zhang, A. Moreo, E. Dagotto, and S. Dong, Frustrated Dipole Order Induces Noncollinear Proper Ferroelectricity in two Dimensions, *Phys. Rev. Lett.* **123**, 067601 (2019).
- [19] Y. L. Jia, M. Zhao, G. Y. Gou, X. C. Zeng, and J. Li, Niobium oxide dihalides NbOX₂: A new family of two-dimensional van der Waals layered materials with intrinsic ferroelectricity and antiferroelectricity, *Nanoscale Horiz.* **4**, 1113 (2019).
- [20] K. Chang, J. Liu, H. Lin, N. Wang, K. Zhao, A. Zhang, F. Jin, Y. Zhong, X. Hu, W. Duan, Q. Zhang, L. Fu, Q. Xue, X. Chen, and S. Ji, Discovery of robust in-plane ferroelectricity in atomic-thick SnTe, *Science* **353**, 274 (2016).
- [21] Y. Zhou, D. Wu, Y. Zhu, Y. Cho, Q. He, X. Yang, K. Herrera, Z. Chu, Y. Han, M. C. Downer, H. Peng, and K. Lai, Out-of-plane piezoelectricity and ferroelectricity in layered α -In₂Se₃ nanoflakes, *Nano Lett.* **17**, 5508 (2017).
- [22] V. M. Fridkin, Bulk photovoltaic effect in noncentrosymmetric crystals, *Crystallogr. Rep.* **46**, 654 (2001).
- [23] M. Nakamura, S. Horiuchi, F. Kagawa, N. Ogawa, T. Kurumaji, Y. Tokura, and M. Kawasaki, Shift current photovoltaic effect in a ferroelectric charge-transfer complex, *Nat. Commun.* **8**, 281 (2017).
- [24] T. Morimoto and N. Nagaosa, Topological aspects of nonlinear excitonic processes in noncentrosymmetric crystals, *Phys. Rev. B* **94**, 035117 (2016).
- [25] J. Spanier, V. Fridkin, A. Rappe, A. Akbashev, A. Polemi, Y. Qi, Z. Gu, S. Young, C. Hawley, and D. Imbrenda, Power conversion efficiency exceeding the Shockley-Queisser limit in a ferroelectric insulator, *Nat. Photonics* **10**, 611 (2016).
- [26] S. Young and A. Rappe, First Principles Calculation of the Shift Current Photovoltaic Effect in Ferroelectrics, *Phys. Rev. Lett.* **109**, 116601 (2012).
- [27] S. Young, F. Zheng, and A. Rappe, First-Principles Calculation of the Bulk Photovoltaic Effect in Bismuth Ferrite, *Phys. Rev. Lett.* **109**, 236601 (2012).
- [28] Z. Gao, X. Dong, N. Li, and J. Ren, Novel two-dimensional silicon dioxide with in-plane negative poisson's ratio, *Nano Lett.* **17**, 772 (2017).
- [29] Q. L. Sun, Y. D. Ma, and N. Kioussis, Two-dimensional Dirac spin-gapless semiconductors with tunable perpendicular magnetic anisotropy and a robust quantum anomalous Hall effect, *Mater. Horiz.* **7**, 2071 (2020).
- [30] S. Woo, H. C. Park, and Y.-W. Son, Poisson's ratio in layered two-dimensional crystals, *Phys. Rev. B* **93**, 75420 (2016).
- [31] L. Meng, Y. Zhang, M. Zhou, J. Zhang, X. Zhou, S. Ni, and W. Wu, Unique zigzag-shaped buckling Zn₂C monolayer with strain-tunable band gap and negative poisson ratio, *Inorg. Chem.* **57**, 1958 (2018).
- [32] S. Shen, Y. Ma, H. Wang, B. Huang, and Y. Dai, Single-layer PtI₂: A multifunctional material with promising photocatalysis toward the oxygen evolution reaction and negative poisson's ratio, *ACS Appl. Mater. Interfaces* **11**, 31793 (2019).
- [33] R. Peng, Y. Ma, Z. He, B. Huang, L. Kou, and Y. Dai, Single-Layer Ag₂S: A Two-dimensional bidirectional auxetic semiconductor, *Nano Lett.* **19**, 1227 (2019).
- [34] Y. Wang, F. Li, Y. Li, and Z. Cheng, Semi-metallic Be₅C₂ monolayer global minimum with quasi-planar pentacoordinate carbons and negative Poisson's ratio, *Nat. Commun.* **7**, 11488 (2016).
- [35] H. Wang, X. Li, P. Li, and J. Yang, δ -Phosphorene: A two dimensional material with a highly negative Poisson's ratio, *Nanoscale* **9**, 850 (2017).
- [36] W. Kohn and L. J. Sham, Self-consistent equations including exchange and correlation effects, *Phys. Rev.* **140**, A1133 (1965).
- [37] G. Kresse and J. Furthmüller, Efficient iterative schemes for Ab initio total-energy calculations using a plane-wave basis set, *Phys. Rev. B* **54**, 11169 (1996).
- [38] J. P. Perdew, K. Burke, and M. Ernzerhof, Generalized Gradient Approximation Made Simple, *Phys. Rev. Lett.* **77**, 3865 (1996).
- [39] S. Grimme, S. Ehrlich, and L. Goerigk, Effect of the damping function in dispersion corrected density functional theory, *J. Comput. Chem.* **32**, 1456 (2011).
- [40] J. Heyd, G. Scuseria, and M. Ernzerhof, Hybrid functionals based on a screened Coulomb potential, *J. Chem. Phys.* **118**, 8207 (2003).

- [41] D. Sheppard, P. Xiao, W. Chemelewski, D. D. Johnson, and G. Henkelman, A generalized solid-state nudged elastic band method, *J. Chem. Phys.* **136**, 074103 (2012).
- [42] A. Togo and I. Tanaka, First principles phonon calculations in materials science, *Scr. Mater.* **108**, 1 (2015).
- [43] See the Supplemental Material at <http://link.aps.org/supplemental/10.1103/PhysRevApplied.15.014027> for more computational details and results of the total polarization as a function of normalized displacement, the corresponding minimum-energy-pathway trajectory for domain-wall motion, the partial charge density, electronic structures, the mechanical response, and optical properties.
- [44] J. Wang, S. Yip, S. Phillpot, and D. Wolf, Crystal Instabilities at Finite Strain, *Phys. Rev. Lett.* **71**, 4182 (1993).
- [45] A. Suleiman, P. Huang, B. Jin, J. Jiang, X. Zhang, X. Zhou, and T. Zhai, Space-confined growth of 2D InI showing high sensitivity in photodetection, *Adv. Electron. Mater.* **2000284**, 1 (2020).
- [46] B. Xu, H. Xiang, Y. Xia, K. Jiang, X. Wan, J. He, J. Yin, and Z. Liu, Monolayer AgBiP₂Se₆: An atomically thin ferroelectric semiconductor with out-plane polarization, *Nanoscale* **9**, 8427 (2017).
- [47] J. Zhang, L. Lin, Y. Zhang, M. Wu, B. Yakobson, and S. Dong, Type-II multiferroic Hf₂VC₂F₂ MXene monolayer with high transition temperature, *J. Am. Chem. Soc.* **140**, 9768 (2018).
- [48] S. Guan, C. Liu, Y. Lu, Y. Yao, and S. Yang, Tunable ferroelectricity and anisotropic electric transport in monolayer β -GeSe, *Phys. Rev. B* **97**, 144104 (2018).
- [49] A. Bruce, Structural phase transitions. II. Static critical behavior, *Adv. Phys.* **29**, 111 (1980).
- [50] J. Hong and D. Vanderbilt, Mapping the energy surface of PbTiO₃ in multidimensional electric-displacement space, *Phys. Rev. B* **84**, 115107 (2011).
- [51] B. Xu, H. Xiang, J. Yin, Y. Xia, and Z. Liu, A two-dimensional tetragonal yttrium nitride monolayer: A ferroelastic semiconductor with switchable anisotropic properties, *Nanoscale* **10**, 215 (2018).
- [52] M. Long, L. Tang, D. Wang, Y. Li, and Z. Shuai, Electronic structure and carrier mobility in graphdiyne sheet and nanoribbons: Theoretical predictions, *ACS Nano* **5**, 2593 (2011).
- [53] L. Li, Y. Yu, G. Ye, Q. Ge, X. Ou, H. Wu, D. Feng, X. Chen, and Y. Zhang, Black phosphorus field-effect transistors, *Nat. Nanotechnol.* **9**, 372 (2014).
- [54] B. Radisavljevic, A. Radenovic, J. Brivio, V. Giacometti, and A. Kis, Single-layer MoS₂ transistors, *Nat. Nanotechnol.* **6**, 147 (2011).
- [55] J. Chen, J. Xi, D. Wang, and Z. Shuai, Carrier mobility in graphyne should be even larger than that in graphene: A theoretical prediction, *J. Phys. Chem. Lett.* **4**, 1443 (2013).
- [56] S. Lalitha, S. Karazhanov, P. Ravindran, S. Senthilarasu, R. Sathyamoorthy, and J. Janabergenov, Electronic structure, structural and optical properties of thermally evaporated CdTe thin films, *Phys. B* **387**, 227 (2007).
- [57] M. Bernardi, M. Palummo, and J. Grossman, Extraordinary sunlight absorption and one nanometer thick photovoltaics using two-dimensional monolayer materials, *Nano Lett.* **13**, 3664 (2013).
- [58] E. Cadelano, P. L. Palla, S. Giordano, and L. Colombo, Elastic properties of hydrogenated graphene, *Phys. Rev. B* **82**, 235414 (2010).
- [59] C. Lee, X. Wei, J. W. Kysar, and J. Hone, Measurement of the elastic properties and intrinsic strength of monolayer graphene, *Science* **321**, 385 (2008).
- [60] Y. Cai, G. Zhang, and Y. W. Zhang, Polarity-reversed robust carrier mobility in monolayer MoS₂ nanoribbons, *J. Am. Chem. Soc.* **136**, 6269 (2014).
- [61] S. Zhao, Z. Li, and J. Yang, Obtaining two-dimensional electron gas in free space without resorting to electron doping: An electride based design, *J. Am. Chem. Soc.* **136**, 13313 (2014).
- [62] M. Topsakal and S. Ciraci, Elastic and plastic deformation of graphene, silicene, and boron nitride honeycomb nanoribbons under uniaxial tension: A first-principles density-functional theory, *Phys. Rev. B* **81**, 024107 (2010).